A new generation of metal chillers to control the solidification structure of Al-4.5 wt%Cu alloy

Zohrehsadat Noohi [a], Behzad Niroumand [a,*], Masoud Panjepour [a], Giulio Timelli [b]

[a] Department of Materials Engineering, Isfahan University of Technology, 84156-83111, Isfahan, Iran
[b] Department of Management and Engineering, University of Padova, Stradella S. Nicola, 3 I-3600 Vicenza, Italy

A R T I C L E I N F O

A B S T R A C T

This paper introduces and examines a new generation of chillers for judicious control of the solidification structure of cast metals and alloys. This innovative chiller makes use of the absorption of the latent heat of melting of a Phase Change Material (PCM) incorporated in the chiller. In this work, Al-4.5 wt%Cu melt was cast in sand molds fitted with a traditional solid steel chiller as well as this new type of chiller consisted of a steel container filled with a given amount of pure zinc as PCM. Effects of the PCM fitted chiller on the thermal history, solidification and structure of the castings were studied by experimental and computer simulation investigations. The optimum casting parameters and mold and chillers dimensions were selected using ProCast simulation software. Use of the PCM fitted chiller resulted in faster columnar-equiaxed transition, 27 %, 54 % and 40 % reduction in the length of the columnar zone and the primary and the secondary dendrite arm spacings, respectively, and about 30 % improvement in the hardness. Thermal gradients and cooling rates at different points of the PCM fitted casting were generally more than those in the traditionally chilled casting. Use of the PCM fitted chiller eliminated the formation of the feathery grains and reduced the formation of the undesired Fe-rich phases close to the chiller due to different thermal history of the castings. Segregation pattern and change of Growth Restriction Factor (GRF) along the castings were studied and related to the cooling and growth conditions experienced by each casting.

1. Introduction

Aluminum alloys are utilized in various applications such as in automobile, aerospace, and sports industries because of their unique properties including light weight, high thermal and electrical conductivity, and good corrosion resistance, castability, and strength [1,2]. It is known that solidification structure greatly affects the mechanical and physical properties of the castings. Therefore, various methods such as grain refinement [3–5], control of cooling rate [3,6], directional solidification [7,8], squeeze casting [9,10], semisolid casting [11,12], applying electric field [13], and manipulating the growth restriction factor (GRF) [14] have been employed to control the solidification structure of the castings.

The formation of chill, columnar and equiaxed grains zones in castings of many different alloys have been well studied [15]. While a columnar structure may be preferred in some applications such as in turbine blades and single crystal manufacturing, isotropic properties of equiaxed grains make it the desired structure in the majority of

engineering applications. As a result, the Columnar to Equiaxed Transition (CET) phenomenon has been widely investigated and many methods have been introduced to control its occurrence [16,17]. The basis of all these methods is to encourage grain nucleation and growth ahead of the solidification front. The use of metallic chillers is a popular method to promote CET and at the same time induce directional solidification, increase feeding distance and improve the integrity of the castings [18].

GRF is another parameter that controls the equiaxed grain nucleation in front of the columnar grains. $mC_0(k_0-1)$ is the typical relationship presented for the calculation of GRF for a binary alloy. Of course, the calculation of GRF in ternary and more complicated alloy systems becomes difficult as accurate estimation of m and k_0 values in these systems is not an easy task. A new method proposed by Schmid-Fetzer and Kozlov [19] for the calculation of GRF of complex alloys systems will be explained in the next section. GRF underlines the potential of an alloy for the formation of a concentration layer of solute elements in front of the solid/liquid interface to increase the constitutional undercooling (ΔT_C) and promote the equiaxed grains nucleation. Grain size has been

List of symbols and acronyms

Δt	Time difference (s)
ΔT_C	Constitutional undercooling (°C)
C_O	Solute content of the alloy
C_S	Solute content of the last solid formed on the solid-liquid interface
D	Diffusion coefficient of solute in the melt
f_s	Solid fraction
g	Gram
G	Thermal gradient (°C/mm)
k_0	Equilibrium partition coefficient of the binary phase
m	Liquidus slope of the phase diagram
R	Growth rate of the solidification front (mm/s)
s	Second
t_{TL}	Time of cooling from T_L (s)
t_{TL-2}	Time of cooling from T_L-2 (s)
T_E	Eutectic temperature (°C)

T_L	Liquidus temperature (°C)
T_m	Melting temperature (°C)
CAFE	Cellular Automation Finite Element
CET	Columnar to Equiaxed Transition
C.R.	Cooling Rate
EDS	Energy Dispersive X-ray
EDWC	Electrical Discharge Wire Cut
HTC	Heat Transfer Coefficient
GRF	Growth Restriction Factor
OES	Optical Emission Spectroscopy
PCM	Phase Change Material
PDAS	Primary Dendrite Arm Spacing
Q	Growth Restriction Factor
SDAS	Secondary Dendrite Arm Spacing
SEM	Scanning Electron Microscope
SES	Spark Emission Spectroscopy
TES	Thermal Energy Storage

reported to decrease by increasing GRF [20].

In the current paper, use of a new generation of metal chillers including a metallic container filled with a PCM has been proposed to control the solidification structure and occurrence of CET. PCM is a material that releases and absorbs some latent heat during its solidification and melting at a relatively constant transition temperature. So far, PCMs have been mainly used in Thermal Energy Storage (TES) applications in solar energy systems [21], buildings [22], and electronic devices [23]. PCMs have been classified into organic, inorganic and eutectic materials. Metallic PCMs can be categorized according to their melting temperature into low ($T_m < 420$ °C), medium (420 °C $< T_m <$ 1000 °C) and high melting temperatures ($T_m > 1000$ °C) [24].

In this paper, an innovative chiller consisting of a steel container filled with Zn as PCM was designed and used to control the solidification structure of an Al-4.5 wt%Cu alloy. The cooling, growth and structural characteristics of the castings made using the innovative chiller and a conventional steel chiller of a similar cooling capacity were investigated and compared with the traditionally chilled casting.

2. Materials and methods

In this study two types of directionally solidified Al-4.5 wt%Cu castings were made; one using a traditional solid steel chiller and the other using a new type of chiller consisting of a steel container filled with a predetermined amount of a metallic PCM. For the sake of brevity, from here on in this paper, the former is called "Chill casting" and the latter is called "PCM casting".

2.1. Materials and molds

Al-4.5 wt%Cu alloy used in this study was produced by melting measured quantities of a commercially pure aluminum ingot and copper electric wires in a resistance furnace. The chemical composition of the alloy as measured by OES (ARL 3460, Switzerland) is shown in Table 1.

Pure zinc was selected as the PCM because of its appropriate melting temperature and high latent heat of melting (26.2 cal/g) [25]. The solid chiller and the container of the PCM (pure zinc) were made of St37 low carbon steel (DIN 17100). Dimensions of the solid chiller and the steel

Table 1
Measured chemical composition of the Al–Cu alloy used in this study.

Elements	Al	Cu	Fe	Other elements
Wt%	Bal.	4.5	0.35	<0.17

container are shown in Fig. 1 and were selected based on computer simulation of the thermal and solidification history of both castings. For making the PCM fitted chiller, first one side of the container was welded close by a steel plate, the container was cleaned and dried and the molten pure zinc was poured into it. The molten zinc was solidified in a directional solidification fashion to avoid the formation of shrinkage defects in the PCM. Subsequently, the excess zinc was milled and a second steel plate was welded to close the container and protect the pure zinc from oxidation and leakage during melting.

Molds were made out of sodium silicate bonded silica sand hardened by CO_2 gas. Schematics and dimensions of the molds as well as the chilling, running and feeding systems are shown in Figs. 1 and 2. Dimensions of the mold cavity were 70 × 30 × 30 mm. Four sides of the mold cavities were insulated by 13 mm alumina insulator boards to promote directional solidification from the chillers to the risers and provide time for melting of the PCM before the solidification of the cast alloy progresses too much.

Selected thermophysical properties of pure zinc [25], St37 steel and the alumina insulator [26] are presented in Table 2. It is noteworthy that the reported properties are some typical values of the given properties to indicate the overall differences of the materials. However, these thermophysical properties are often temperature dependent and, in fact, the temperature dependent properties of the PCM and the steel chiller extracted from the databases of the software were used in the Procast simulations. Thermophysical properties of the insulator material in the temperature range of interest in this work were considered to be constant.

Both chill and PCM castings were cast at 750 °C. Each experiment was repeated twice. Three calibrated K-type thermocouples were placed into the central longitude section of each casting 10, 35 and 60 mm from the chiller surfaces. One thermocouple was placed in the center of the solid steel chiller and two thermocouples were placed in the middle of the front and back sides of the pure zinc as shown in Figs. 1 and 2. Thermal history of these points were recorded using a data-logger at a sample rate of 1 s^{-1}.

2.2. Thermal and solidificatuon simulations

Thermal and solidification histories in both castings were simulated using ProCast simulation software version 2018. Mesh analyses were performed and the optimum tetrahedral meshes found for different parts of the castings and molds are presented in Table 3. Following some preliminary casting experiments, the measured thermal histories at different points of the castings were used to calibrate the simulation
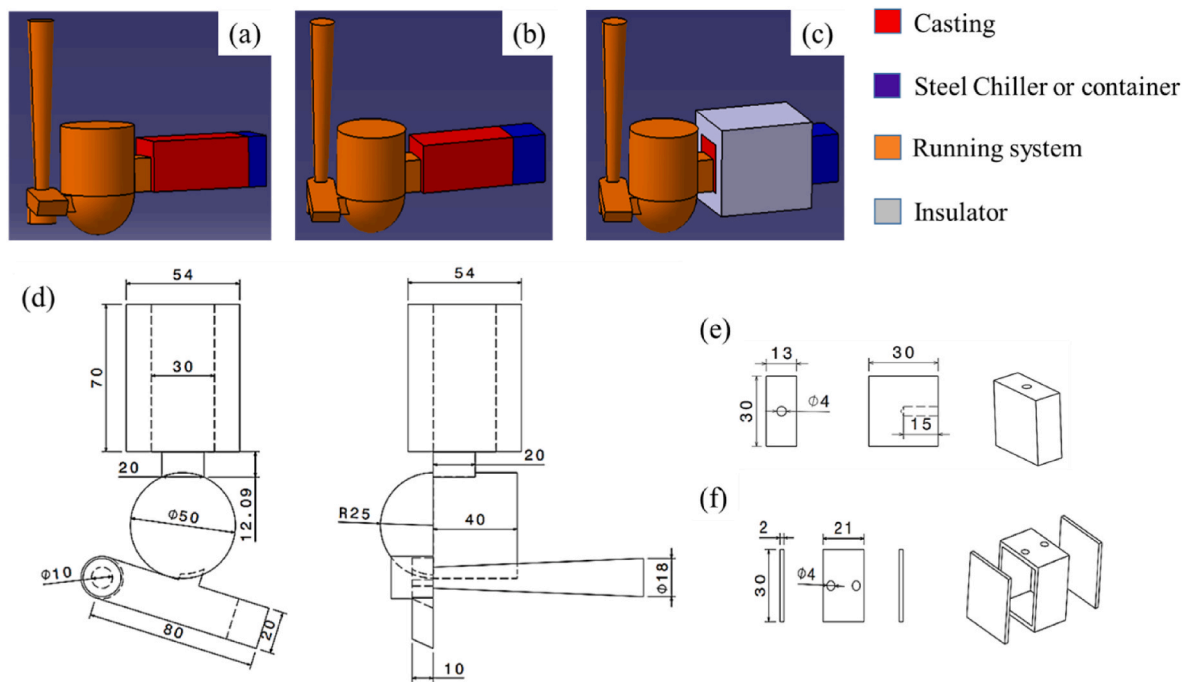
Fig. 1. 3D schematic of a) Chill casting (insulator removed), b) PCM casting (insulator removed) and c) Chill or PCM casting (insulator shown). Dimensions (mm) of d) casting, running and feeding systems, e) solid steel chiller for Chill casting and f) steel container for PCM casting.
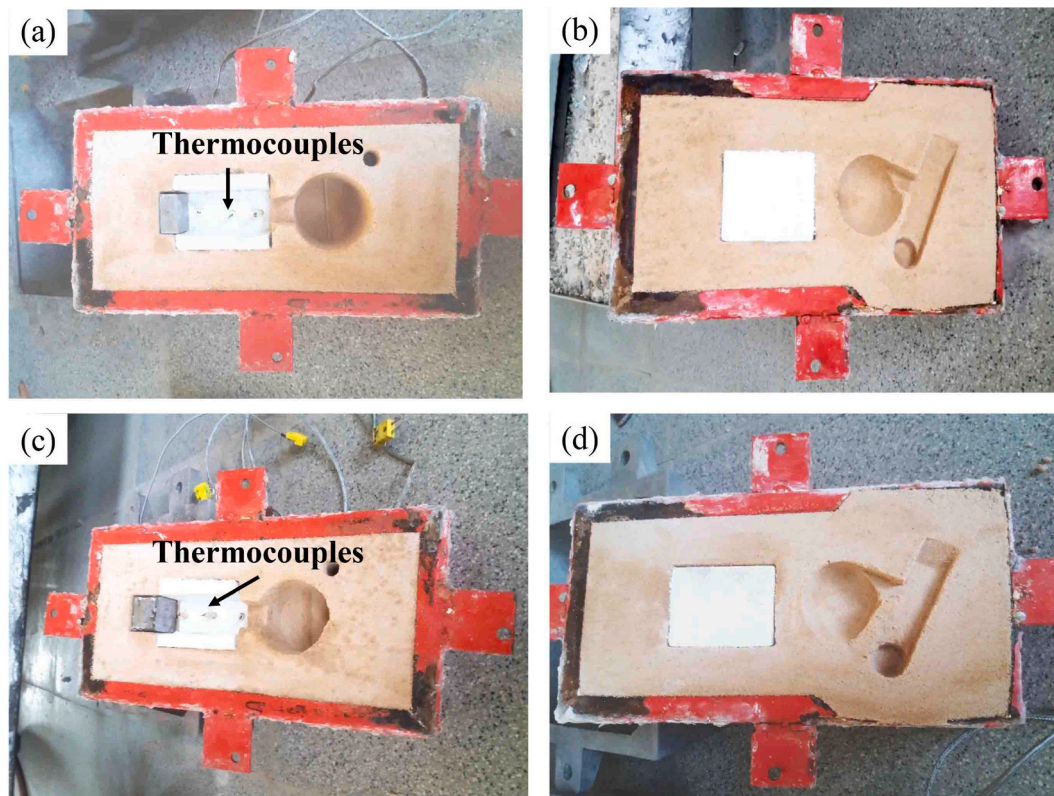

Fig. 2. Photographs of a) cope and (b) drag flasks of Chill casting and c) cope and d) drag flasks of PCM casting.

boundary conditions. Consequently, the Heat Transfer Coefficients (HTCs) between different parts of the molds and the castings were selected in accordance with Table 4.

Dimensions of the casting, running and feeding systems, solid chiller, PCM and its steel container, and the insulator, as shown in Fig. 1, as well

as the casting conditions (pouring temperature of 750 °C and mass flow of 200 g/s) were selected after multiple simulations using the calibrated software.

Subsequently, thermal history and the cooling rate at different co-ordinates of the castings, solid chill, steel container or PCM, as well as

Table 2
Typical thermophysical properties of pure zinc, St37 steel and alumina insulator [25,26].

	T_m (°C)	K (W/m K)	C_P (J/kg K)	ρ (kg/m³)	α (m²/s)
Pure zinc	419.5	119.5	394	7140	4.2×10^{-5}
Steel	–	54	465	7833	1.5×10^{-5}
Alumina	–	22	834	3864	6.8×10^{-6}

the thermal gradient (*G*) and growth rate (*R*) of the solidification interface and grain size and macrostructure of the castings were analyzed using the simulation results (Fig. 3). Time-temperature (T-t) diagrams were obtained in 1 mm spacings in the central longitude axis of the castings from the chillers surface to the running system (71 points in total for each casting).

Average *G* and *R* values were calculated at 10 mm distances using these data. At each 10 mm, first, the time when the temperature of that point reached the liquidus temperature of Al-4.5 wt%Cu alloy was found. Subsequently, the temperature at the next 9 nodes (10 mm) was determined at this given time. Using these data, the Temperature-Distance (T-x) diagram for each point was developed and *G* in front of the solidification front was calculated as the slope of the curve. *R* at each point was calculated according to Eq. (1), where *Δt* (s) is the difference between the time when the first and the last node in every 10 mm spacing reached to the liquidus temperature of the cast alloy.

$$R = 10/\Delta t \ (\mathrm{mm/s}) \tag{1}$$

The cooling rate (*C.R.*) at any given point of the castings was calculated using its corresponding T-t diagram. First, the liquidus temperature (*T_L*) of the alloy was determined from the recoalescence or change of slope of the diagram. *C.R.* was then calculated according to Eq. (2) in the following 2 °C temperature drop, i.e. T_L to T_L-2 (°C).

$$C.R. = 2 / \left(t_{(TL)} - t_{(TL-2)} \right) \ (°C/s) \tag{2}$$

Progress of the solidification front with time was studied by determining the time when the temperature of each of the points shown in Fig. 3 reached its T_L and T_E. In addition, macrostructures of the castings were simulated using the CAFE module of the ProCast software.

Local GRFs of the structures were calculated using Eq. (3) and according to the method introduced by Schmid-Fetzer and Kozlov [19] for ternary and more complex alloys. In this method, variation of the ΔT_C with a solid fraction (f_S) for f_S of 0–0.01 and ΔT_C of 0–1 °C is plotted and

fitted by a quadratic function as shown in Eq. (4). *b* constant in this equation will be equal to the GRF of the composition.

$$Q = \left(\frac{d\Delta T_C}{df_s} \right)_{f_s \to 0} \tag{3}$$

$$\Delta T_{CS} = a + b.f_s + c.f_s^2 , \quad 0 < f_s < 0.01 \ and \ 0 < \Delta T_{CS} < 1 \ °C \tag{4}$$

The required T-f_S curves of different compositions were plotted using Thermo-Calc software version 2016.

2.3. Macro and microstructure observations

Each casting was electrical discharge wire cut (EDWC) in half in a vertical longitude direction. One of the sections was ground on silicon carbide (SiC) papers to 600 grit and etched by Keller etchant for about 2 min to reveal the macrostructure of the samples. Due to the large size of the grains, they were examined by an OPTIKA stereoscope. The average equivalent diameter of the equiaxed grains and the average length of the columnar grains were measured by ImageJ software. The microstructure and chemical composition of intermetallic phases and solute segregation in the castings were studied using a Seron ALS2300 scanning electron microscope (SEM) equipped with an energy dispersive X-ray (EDS) spectroscope.

2.4. Mechanical properties

Brinell hardness tests were performed on an AMSLER hardness testing machine at a load of 62.5 kg using a 2.5 mm diameter indenter. The average hardness of each casting as well as the hardness profile along the length of the castings at 5 mm spacings were recorded.

3. Results and discussion

3.1. Callibration of the simulation software

The experimentally obtained T-t diagrams at 3 points in each casting, one point in the solid chiller and 2 points in the PCM, as described in sections 2.1, are shown in Fig. 4 (solid lines) for Chill and PCM castings. Rapid temperature increase to the pouring temperature followed by cooling is observed at all the 3 distances from the chiller surfaces. Clearly, the cooling is faster at points closer to the chillers. Two main slope changes in the cooling curves are observed around 647 and 528 °C,

Table 3
Tetrahedral mesh for different parts of molds and castings.

	Casting	Running system	Insulator	Solid chiller	Steel container	Pure Zinc	Mold
Tetrahedral No.	209517	124499	285639	17078	43510	71214	43190

Table 4
HTCs (W/m²K) between different parts of molds and castings.

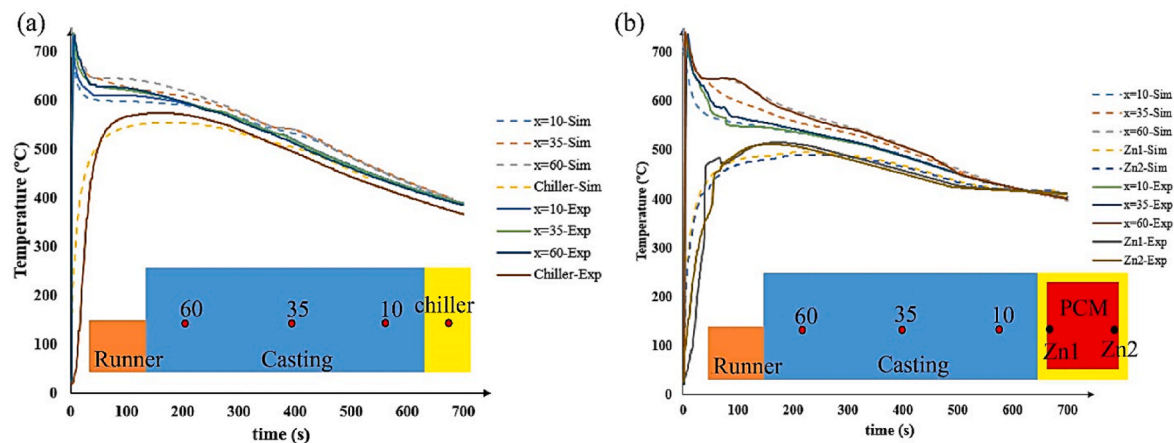|	Casting/Mold	Casting/Chiller	Casting/Insulator	Running system/Mold	Chiller/Mold	Insulator/Mold	PCM/steel container
Chill casting	200	3000–4000	50	200	100	20	–
PCM casting	200	5000–6000	50	200	100	20	1000–4500

Fig. 3. Schematic of (a) Chill and (b) PCM samples in longitudinal section of samples.

Fig. 4. Simulation and experimental T-t diagrams of (a) Chill and (b) PCM casting.

which are related to the liquidus and eutectic temperatures of the alloy, respectively.

In the center of the solid steel chiller, the experimentally measured temperature increases less rapidly to a maximum of 575 °C and cools down very slowly (Fig. 4a). In the PCM, the experimentally measured temperatures increase to the melting point of PCM (pure Zn) where a thermal arrest is observed (inset in Fig. 4b) and then they increase to a maximum of 515 °C. Some fluctuations in the curves are believed to be due to poor thermocouple-PCM contact before the PCM is melted.

Simulated T-t diagrams at the mentioned coordinates are also shown in Fig. 4 (broken lines). The curves were obtained after several adjustments to the boundary conditions, especially to the HTC of different interfaces, until an acceptable agreement between the simulation and experimental data was found. HTC values reported in Table 4 are the results of this effort to calibrate the simulation with the experimental data. The calibrated simulation conditions were then used for the thermal simulation of other points in the castings.

In the simulated curves of the PCM, the temperature of pure zinc at Zn1 and Zn2 positions (Fig. 4b) reaches 419.5 °C after 35 and 45 s, respectively. Pure zinc starts to melt and absorb its required latent heat from the cast alloy. After the completion of melting of zinc at each point, its temperature increases to about 500 °C. A small slope change at 419.5 °C related to the melting of the PCM is detected in both simulated curves too. Due to the rapid heating of the PCM, melting at these points is completed rapidly. Subsequent solidification of the PCM at longer times (about 500 s), resulting in a long and more clear thermal arrest, is also evident from the simulated curves.

According to the simulation curves, complete solidification times for Chill and PCM castings are about 440 and 380 s, respectively, which underlines the stronger cooling capacity of the innovative chiller.

3.2. Comparison criteria

The main idea behind implanting a PCM in a traditional chiller is to utilize the melting of the PCM at a predetermined stage of solidification of the cast alloy to absorb a given amount of heat, therefore, affecting the cooling rate as well as the solidification and structure of the cast alloy in a premeditated manner. To isolate the effects of melting of PCM on cooling and solidification of the PCM casting, it was thought that melting of the PCM (pure zinc) should occur before complete solidification of the cast alloy (Al-4.5 wt%Cu), preferably when the solidification front is about the middle of the casting. Also, both chillers should have a comparable effect on the cooling and solidification of the cast alloy until the onset of melting of the PCM. To fulfill these requirements, the following two criteria for the design of the two types of chillers were considered.

1. A similar *C.R.* at the cast/chiller interface, and
2. Similar growth of the solidification front (interface) when the melting of the PCM starts.

The finalized design of the castings and chillers as shown in Fig. 1 are the result of numerous design modifications and simulations to satisfy these criteria.

The liquidus temperature, *C.R.*, *G* and *R* values at different times and different points along the central longitudinal section of the castings (Fig. 3) as well as the advancement of the solidification front with time were computed using the simulation data and the procedures described in section 2.2.

The results indicate that the liquidus temperature of the alloy at all locations except those very close to the chillers surfaces was about 647 °C. At the chiller surfaces (x = 0 mm), due to the initial rapid cooling of the alloy, the liquidus temperature was reduced to about 641 °C for both samples. Accordingly, the computed *C.R.s* at different points of the castings (Fig. 3) are presented in Table 5. The similarity of *C.R.* at the interfaces (x = 0 mm) of the optimized chillers is evident from the table. In both castings, the effect of chillers decreases by moving away from chillers. But, except for the two ends of the castings, the *C.R.* of PCM casting is more than that of Chill casting in every other point.

At the early times (corresponding to *x* = 0 mm), the heat transfer at the steel–molten aluminum interface in both chillers seems to be very similar. But, in the later times, *C.R.* differs because of the different thermophysical properties of pure zinc and steel (Table 2). Moreover, in PCM casting, as the PCM (pure Zn) starts to melt and absorb its required latent heat from the molten cast alloy, the innovative chiller consumes extra heat to heat up and, therefore, is not saturated as easily. In other words, it retains its chilling ability for a longer time.

Fig. 5 demonstrates the development of different solidification regions with time for both samples. Five separate temperature regions are detected in this figure, i.e. regions with $T > T_L$, $T = T_L$, $T_E < T < T_L$, $T = T_E$, and $T < T_E$. The results indicate that the growth of the solidification front in both samples is similar up to 35 s after pouring, corresponding to x ≈ 30 mm. At 40 s, the solidification front is at 39 and 32 mm for PCM and Chill castings, respectively, indicating the of accelerated growth in the PCM casting after 35 s. In fact, 35 s corresponds with the time when the first layer of pure zinc starts to melt (Fig. 4). This demonstrates the effect of melting of the PCM on heat absorption by the innovative chiller

Table 5
C.R. of samples at different points.

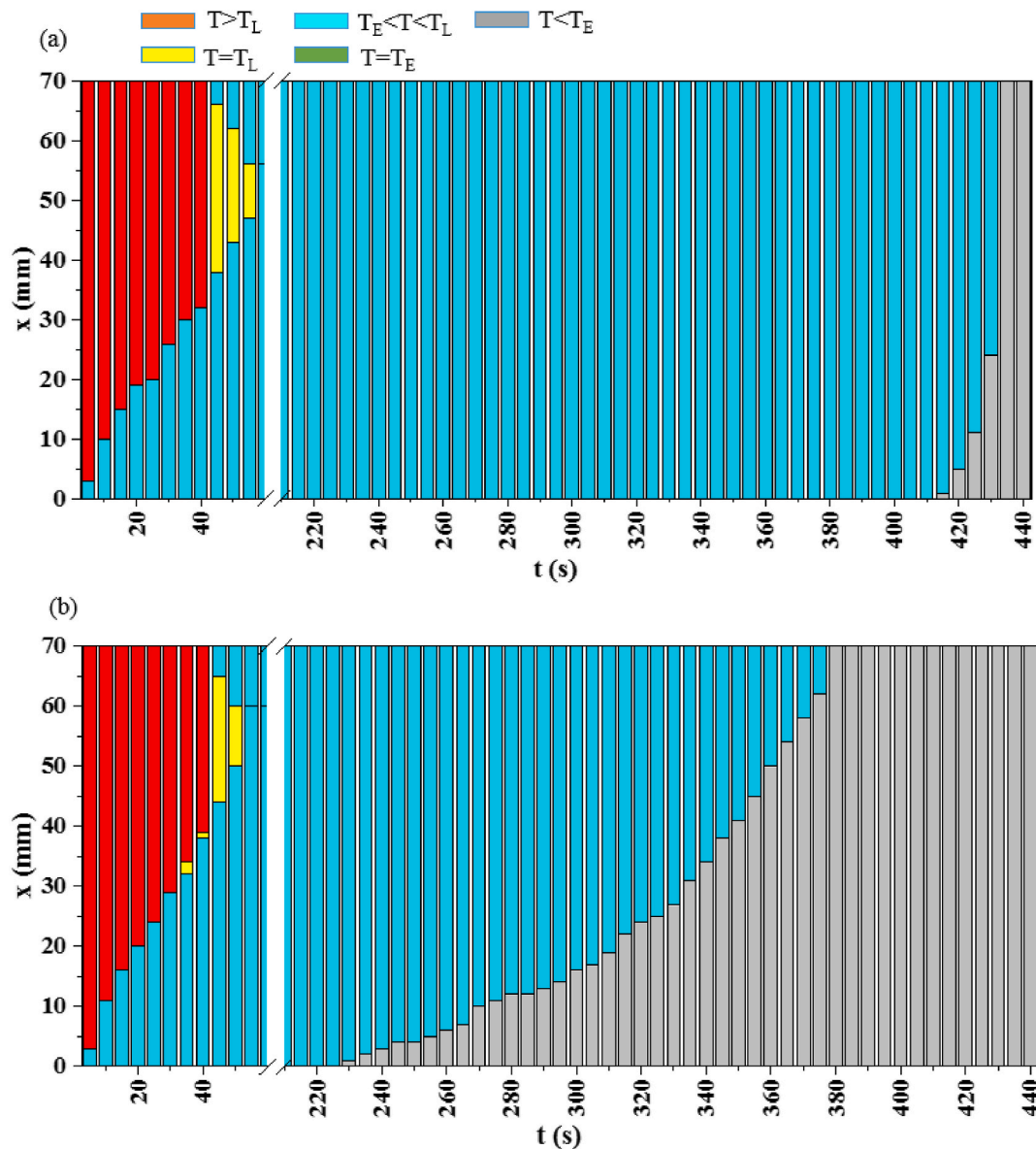| *x* (mm)	0	10	20	30	40	50	60	70
Chill	21	4	1.1	0.5	0.1	0.04	0.03	0.04
PCM	21	5.6	2	1	0.2	0.1	0.04	0.04

Fig. 5. Growth of different solidification regions with time for a) Chill casting and b) PCM casting.

and the ensuing solidification events at $t > 35$ s.

The results indicated that both comparability criteria have been met by the designed chillers. Therefore, the expected differences in the structure of the two samples can be associated with the melting of the implanted PCM.

One logical question that may arise is that while the cooling rate of the innovative chiller is more than that of the solid steel chiller (Table 5), how the similarity of advancement of the solidification front till the melting of the PCM can be explained? This will be addressed in section 3.4.

According to Fig. 5, the completion of solidification of the cast alloy ($T < T_E$) started and finished at 230 and 380 s, respectively, in PCM casting. For Chill casting, this happened between 410 and 440 s. This suggests a more effective directional solidification and less shrinkage defect formation in PCM casting as was observed in metallographic studies [27].

3.3. Thermal simulation of the chillers

Fig. 6 illustrates the development of temperature profiles inside both

chillers at temperatures around the melting temperature of pure zinc (PCM), i.e. 419.5 °C. In Chill casting, the temperature of the whole of the solid steel chiller reaches 419.5 °C before 35 s, and the temperature of the solid steel chiller reaches its maximum of 555 °C after 180 s. Different cooling characteristics of the two chillers are evident from the figure. The different temperature profiles developed after 30 s in the solid steel chiller (Fig. 6a) and PCM fitted chiller (Fig. 6b), respectively, is due to the edge effect in the former and the existing air gap between the container and the solid PCM in the latter. The more rapid heat transfer from the edges and the greater heat influx from the center of the solid chiller result in the displayed curved temperature profile. In the PCM fitted chiller, however, the micrometric air gap between the steel container and the solid PCM before melting impedes the heat transfer across their interface significantly. This results in more rapid temperature increase in the casting side of the steel container as shown in Fig. 6b at t = 15 s. Due to the air gap, the heat transfer before melting of the PCM is only through the four sides of the container as evident from Fig. 6b at t = 30 and 35 s. During this time, the PCM temperature does not increase significantly.

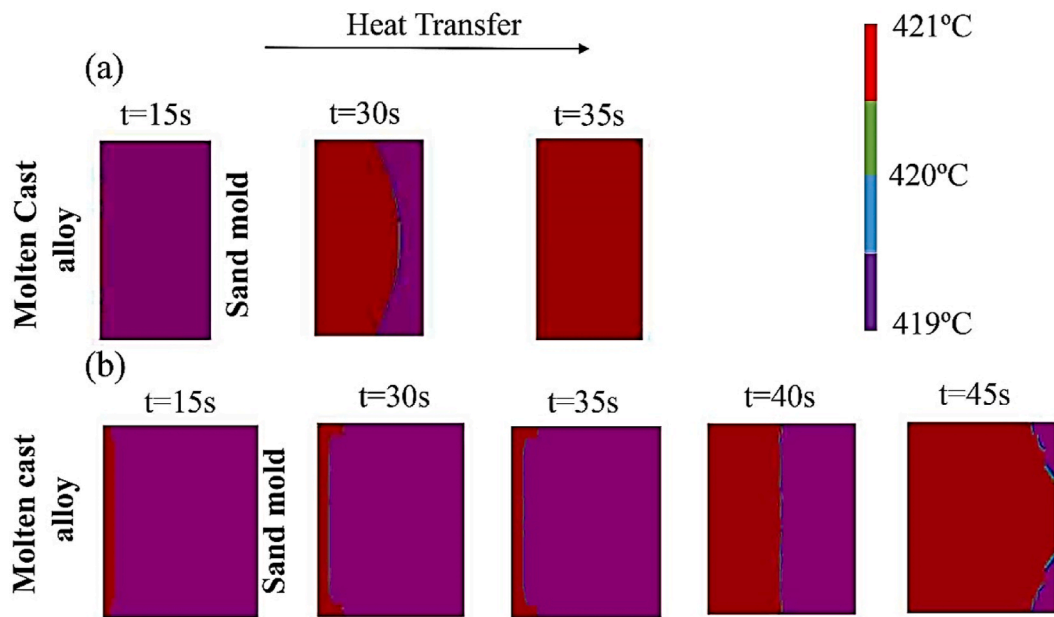Melting of the PCM starts at 35 s resulting in a significantly better

Fig. 6. Temperature profiles in longitudinal section of chillers between 419 and 421 °C: (a) Chill casting and (b) PCM casting.

contact and improved heat transfer between the molten zinc and the steel container. It takes about 10 s for the rest of the PCM to reach the melting point. Melting of the first layer is accompanied by consumption of the heat input from the molten cast alloy and interrupts the directional heat flow toward the far end of the PCM. This is probably the reason for a straight rather curved temperature profile seen in Fig. 6b. The depth of the melted PCM increases during the next 10 s to include all the PCM. Afterward, the continued heat input leads to an increase in PCM temperature to a maximum of 500 °C after 200 s.

It should be emphasized that the heat consumption imposed by melting the PCM in the innovative chiller can postpone the thermal saturation of the chiller and increase its chilling efficiency. Changing the material, wall thickness or heat transfer surfaces of the container as well as the volume and the type of PCM may be utilized to control the start and duration of melting of the PCM and the latent heat it absorbs to judiciously control the solidification conditions and cast microstructure as desired.

3.4. Macro and microstructural investigations

Macrographs of cross sections of Chill and PCM castings are displayed in Fig. 7a and b, respectively, where directional solidification from the chiller towards the running system is evident in both castings. Both castings are comprised of a narrow chill zone close to the chillers, followed by a columnar zone of elongated grains and a region of large equiaxed grains. CET has been marked on both macrostructures. As shown in Fig. 7, CET has occurred sooner in PCM casting, i.e. at x = 35 mm, as compared to x = 48 mm for Chill casting. Earlier CET would lead to less textured structure and more isotropic properties of the as cast alloy which is desired in most structural applications. Without much of a surprise, CET occurrence in the PCM casting relates very closely to the start of the melting of the PCM when the solidification front is at x ∼ 30 mm, as discussed earlier. The reason for this will be discussed in this section.

Micrographs of selected areas of the columnar zone of both castings are shown in Fig. 7c and d, respectively. While normal dendritic columnar grains are observed in PCM casting (Fig. 7d) and c displays the formation of the so-called "feathery" grains in the columnar zone of Chill
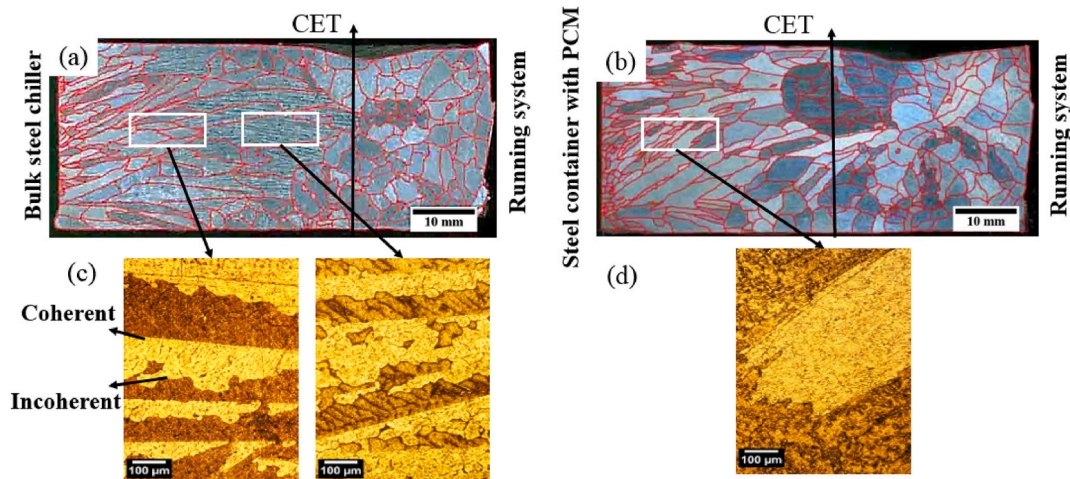

Fig. 7. Macrograph of a) Chill casting and b) PCM casting, and micrograph of (c) Chill casting and (d) PCM casting.

casting before the central equiaxed grains. This is in contrast to some preliminary results of this work with an Al-4.5 wt%Cu-0.2 wt%Fe alloy where the structure of both Chill and PCM castings consisted of conventional chill, columnar and central equiaxed grain zones without any feathery grain formation [2]. In the current work, the iron content of the alloy was increased to promote the feathery grain formation as reported by other researchers [28].

Feathery grains are twinned dendritic structures observed in certain directionally solidified or semi-continuously cast aluminum alloys [29]. They include layers of twinned and untwinned dendrites with coherent {111} twin planes and <110> or <112> directions and faceted interfaces. The structure consists of straight coherent and wavy non-coherent boundaries [30,31]. Growth of feathery grains has been shown to need very small undercooling, therefore they enjoy a high growth rate after nucleation [28].

Feathery grains are generally considered undesirable because they are highly anisotropic, have poor formability, and cannot be eliminated by heat treatment. The mechanism of feathery grains nucleation is not clear yet. However, previous research has shown that they may be formed at high G, high $C.R.$, or high R conditions. Melt convection leading to imposed shear stress to activate the twinned planes, and unfavorable segregation of some elements leading to the formation of certain intermetallic compounds during solidification, are among the possible causes of feathery grains formation [28,30–32]. Inoculation has been reported as one of the few methods to prevent feathery grains formation [29,30,33,34]. Hot rolling of the solidified casting has been also shown to reduce or eliminate the formed feathery grains in some instances [35].

Cu and Fe are the main alloying elements of the cast alloy used in this study (Table 1). Both elements have solute distribution coefficients (k_0) of less than unity in aluminum and, therefore, are segregated in the liquid during solidification. Meng and Chi [33] have reported the formation of feathery grains in an Al–Mg–Si–Cu–Cr–Zr alloy by increasing the Fe content from 0.17 to 0.60 wt%. Rodney et al. [36] have shown that Fe would lead to the anisotropy of solid/liquid interface which promoted the nucleation of feathery grains. Kurtulda et al. [28] have demonstrated that the formation of some icosahedral quasicrystals such as $Al_{45}Cr_7$ in the melt led to feathery grains nucleation in Al-20% WtZn-0.1%WtCr alloy. Such icosahedral quasicrystals as $Al_{62.5}Cu_{24.5}Fe_{13}$ and $A_{64}Cu_{24}Fe_{12}$ can be formed in Al–Cu–Fe alloys and may act as a heterogeneous site for nucleation of twinned α-Al phase [37,38].

Considering the causes of feathery grains formation, since convection and pouring conditions were assumed similar for both castings, G, R and $C.R.$ values were calculated following the procedures described in section 2.2, to investigate their potential influence on the structure. G, R, G/R and $G \times R$ values for different sections of the castings are tabulated in Table 6. It is seen that the regions of $x = 0$–50 mm have positive thermal gradients indicating that they are affected by the chiller heat transfer. At $x = 50$–70 mm, G features a negative value due to the cooling effects of the running system.

According to Table 6, G values are generally higher for PCM casting, due to higher thermal diffusivity and latent heat absorption in this

innovative chiller. $C.R.$, denoted by $G \times R$, is lower in Chill casting at all regions which confirms the results presented in Table 5. R values of both castings are close at $x = 0$–30 mm, which is compatible with the findings of Fig. 4. R values of Chill casting become greater than that of PCM casting at $x = 30$–50 mm. It is believed that since the feathery macrostructure has a high growth rate, it can progress rapidly into molten metal during solidification. Therefore, despite the lower cooling rate in Chill casting, interface growth up to $x = 30$ mm is similar to that of PCM casting. In other words, it is believed that the characteristic higher growth rate of the feathery grains [32] has compensated for the lower $C.R.$ of the Chill casting and led to comparable growth rate and solidification front advancement before melting of the PCM (pure zinc).

As it is observed G/R decreases continuously from the chiller to the running system in PCM casting. This can affect the growth morphology of the grains. In fact, as G/R ratio is reduced, the situation for the formation of equiaxed grains and restriction of columnar growth is improved. On the other hand, the maximum G/R in Chill casting occurs at $x = 10$–20 mm which coincides with the initiation of the feathery macrostructure. It may be postulated that G/R of 4 °C.s/mm^2 is the critical value for the formation of feathery grains. However, this needs further investigation. At $x > 20$ mm, G/R ratio of Chill casting decreases due to the increased growth rate of feathery grains.

3.5. Solute segregation and intermetallic formation

It has been previously reported that formation of certain intermetallic compounds could facilitate the feathery grain formation [37,38]. It has also been shown that formation of intermetallic compounds is significantly affected by solute segregation during growth [39] and that the latter is greatly influenced by the cooling rate of the melt and the growth rate of the solidification front during solidification [40]. Therefore, the effects of solute segregation and icosahedral quasicrystal formation in the structure, as potential causes of feathery grain formation, were investigated by EDS analyses on different areas of both castings.

EDS analyses of typical areas in the castings at $x = 10 \pm 1$ mm, where the feathery structure seems to have initiated in Chill casting, are depicted in Fig. 8. The results show the formation of iron-rich phases in Chill casting where Fe content has even reached to about 17%wt. No such Fe rich phases were detected in PCM casting. In addition, chemical composition of one of the iron-rich intermetallic phases detected in Chill casting was close to Al_5Cu_2Fe phase which is similar to the icosahedral quasicrystal phase previously reported as the cause of feathery grain nucleation in Al–Cu–Fe alloy [38]. Furthermore, Fe has been reported to change the anisotropy of solid-liquid interface and atom adsorption kinetics. Since icosahedral phase has a faceted interface with α-Al grains, the grain will continue this interface with feathery structure. The results suggest Fe segregation and formation of Fe rich phases as one possible cause of feathery grain formation.

To address the difference between the Fe segregation at the grain boundaries of Chill casting and PCM casting, differences in the $C.R.$ and size of the microstructural features of the two castings must be considered. It was shown that the two employed chillers had different $C.R.$s.

Table 6
Calculated solidification parameters for Chill and PCM castings.

x (mm)	G (°C/mm)		R (mm/s)		G/R (°C.s/mm^2)		$G \times R$ (°C/s)	
	Chill	PCM	Chill	PCM	Chill	PCM	Chill	PCM
0–10	5.30	6.01	1.460	1.538	3.627	3.904	7.731	9.241
10–20	3.04	2.94	0.758	0.945	4.017	3.113	2.305	2.78
20–30	1.24	1.63	0.784	0.909	1.571	1.796	0.974	1.484
30–40	0.28	0.58	1.786	1.25	0.159	0.462	0.508	0.724
40–50	0.01	0.02	16	9.009	0.001	0.002	0.146	0.207
50–60	−0.003	−0.002	23.529	83.333	−0.0001	−0.00002	−0.073	−0.175
60–70	−0.04	−0.03	4.762	5.391	−0.008	−0.006	−0.18	−0.17

Location	%	Al	Fe	Cu	Phase
1	wt	93.83	0.31	8.85	Matrix
	atm	97.27	0.16	2.58	
2	wt	43.72	16.96	39.32	Al_5Cu_2Fe
	atm	63.72	11.94	24.33	
3	wt	80.28	3.98	15.74	$Al_{40}Cu_3Fe$
	atm	90.02	2.23	7.75	
4	wt	77.45	4.83	17.71	$Al_{33}Cu_3Fe$
	atm	88.71	2.67	8.62	
5	wt	42.34	0.12	57.54	Al_2Cu
	atm	63.35	0.08	36.56	

Location	%	Al	Fe	Cu	Phase
1	wt	96.31	0.22	3.59	Matrix
	atm	98.39	0.05	1.56	
2	wt	36.55	0.22	63.23	AlCu
	atm	57.56	0.17	42.28	
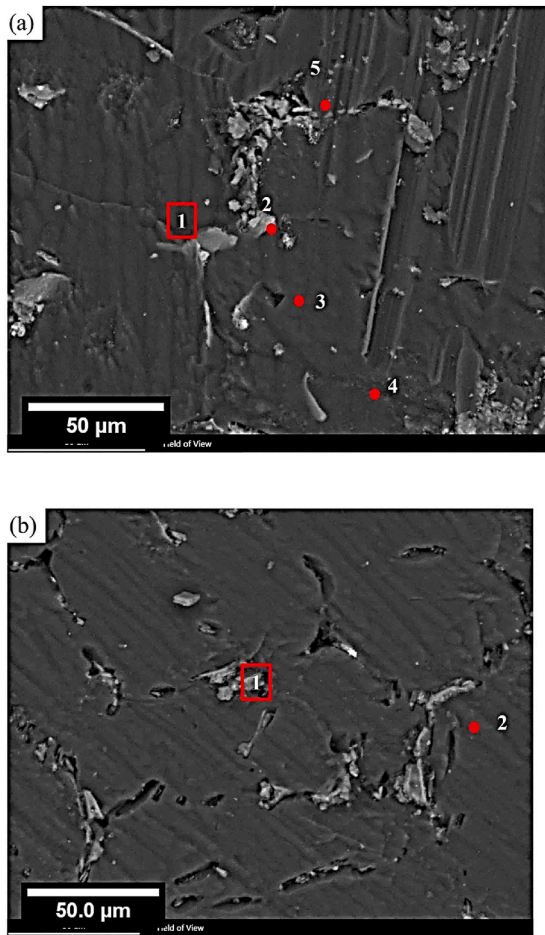
Fig. 8. EDS analyses of (a) Chill casting and (b) PCM casting at x = 10 ± 1 mm.

This could have affected the Fe segregation in the castings. Maximum equilibrium solubility of Fe and Cu in solid Al is reported to be about 0.02 at% at 650 °C [41] and 2.5 at.% at 550 °C (the eutectic temperature) [42], respectively. Due to very low solubility of Fe in the growing aluminum dendrites, Fe atoms are mainly rejected to the melt in front of the growing interface including the grain boundary regions. It is postulated that lower *C.R.* experienced in Chill casting at *x* > 0 mm, allows for greater diffusion of Fe atoms to the grain boundary regions. Sensitivity of Fe segregation to the *C.R.* may be better highlighted considering Fe diffusion coefficient in Al. Diffusion coefficient of Fe in solid Al is a few order of magnitude lower than that of Cu, e.g. about 3.5 $\times 10^{-18}$ m^2/s for Fe in comparison with 4.7 $\times 10^{-13}$ m^2/s for Cu at 600 °C [43]. On the other hand, diffusion coefficient of Fe in liquid Al is also reported to be 50–60 % less than that of Cu [43]. In fact, after rejection from the solid-liquid interface, Fe atoms are more likely to concentrate between the grains whereas Cu atoms have a higher change of diffusing down the concentration gradient towards the opposite side of the mold.

On the other hand, the measured secondary dendrite arm spacing of the columnar portion of Chill casting and PCM casting are 72 ± 5.4 and 43 ± 5 μm, respectively [27]. Effects of microstructural refinement on dilution of solute segregation at grain boundaries has been frequently shown before [44,45]. It is believed that coarser microstructure of Chill casting, accompanied by higher segregation of Fe atoms at its grain boundaries, have facilitated the formation of Fe-rich intermetallic compounds in Chill casting, as evidently shown in Fig. 8.

3.6. Grain size and grain size distribution of equiaxed grains

The average equivalent diameter of the equiaxed grains and its distribution curve, as determined by ImageJ software, is shown in Fig. 9 for both castings. In agreement with Fig. 7a and b, the average equivalent diameter of the equiaxed grains in both castings is similar and about 2.6 ± 1.1 mm. Despite this, the larger equiaxed region in PCM casting, as shown in Fig. 7, and larger number of equiaxed grains (165 in PCM casting compared to 140 in Chill casting) grants stronger isotropic properties for PCM casting.

Macrostructures of the castings were also simulated using CAFE module of the ProCast software and the average size and distribution of the equiaxed grains were measured. The results are shown in Fig. 10. A good agreement is observed between the results of the experimental and simulation studies. According to Fig. 10a and b, CET in Chill casting and PCM casting has occurred at *x* = 48 and *x* = 32 mm, respectively, which is comparable with the experimental results (Fig. 7a and b) where CET in Chill and PCM castings occurred at *x* = 48 and *x* = 35 mm, respectively. Based on Fig. 10, the average size of equiaxed grains for Chill and PCM castings were 2.8 ± 1 and 2.7 ± 0.7 mm, respectively, which are also very close to the experimental measurements of 2.6 ± 1.1 mm. These results confirmed the accuracy of the simulation results. It should be noted that ProCast software cannot simulate the formation of feathery grains and only shows the columnar and equiaxed structures.

3.7. Columnar to equiaxed transition (CET)

It was shown that despite the fact that cooling rate in PCM casting was about twice that in Chill casting, the extent of the columnar zone in
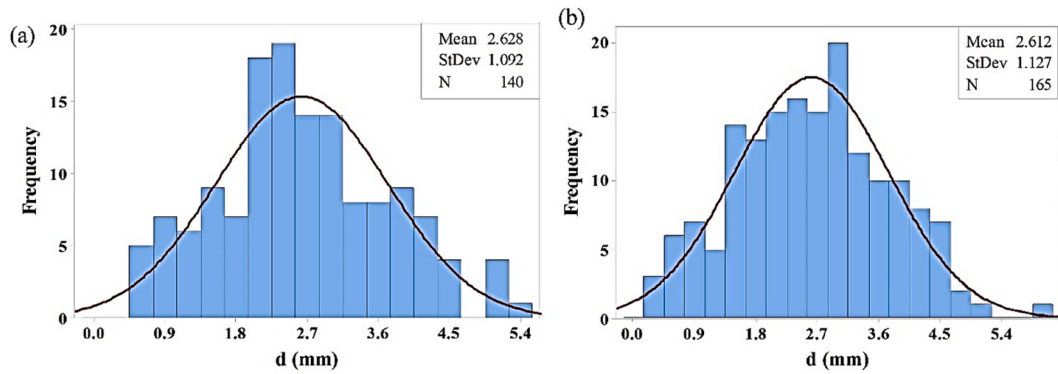
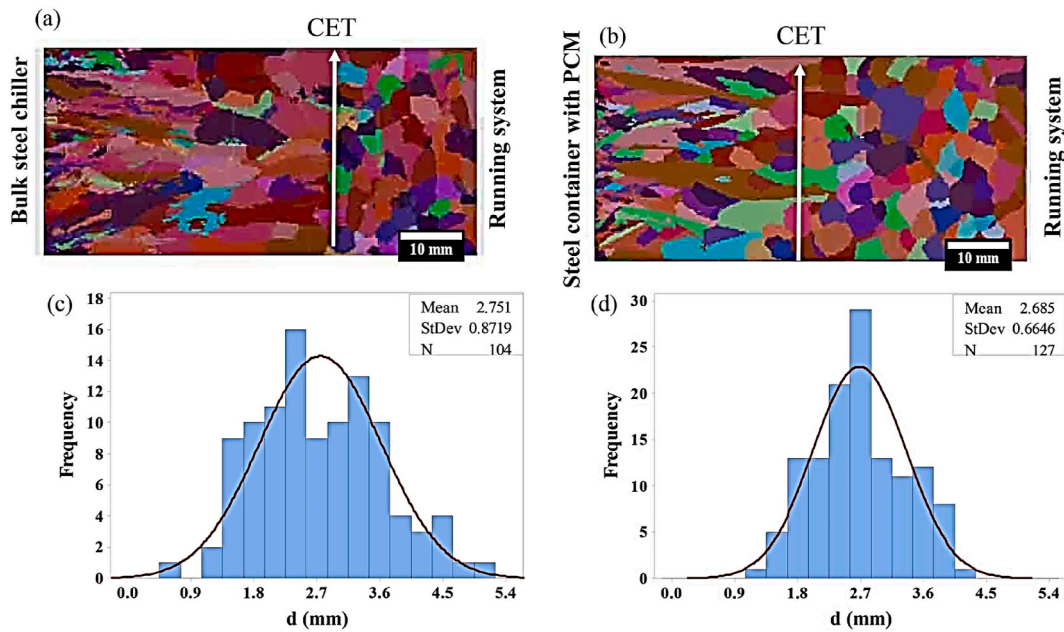**Fig. 9.** Grain size distribution of (a) Chill casting and (b) PCM casting.

Fig. 10. Simulated macrostructure of a) Chill casting and b) PCM casting, and grain size distribution of c) Chill casting and d) PCM casting.

PCM casting was smaller and CET occurred earlier than that in Chill casting. This was related to the start of melting of the PCM (pure Zn) and increased heat absorption when the solidification front has reached to x = 30 mm. Reduction of G/R from the chillers towards the end of both castings is evident from Table 6. As mentioned before, decreased *G/R* would result is shorter columnar zone. CET has occurred at 48 and 35 mm from the chillers in Chill casting and PCM casting, respectively, which corresponds to *G/R* value of about 0.001 °C.s/mm² at 40–50 mm for Chill casting and 0.462 °C.s/mm² at 30–40 mm for PCM casting.

Larger columnar zone and later occurrence of CET in Chill casting is thought to be due to the changes in growth morphology, constitutional undercooling and GRF of the growing solid-liquid interface brought about by incorporation of the PCM into the chiller used in PCM casting.

3.7.1. Morphology

Despite the imposed directional solidification in the molds and concurrent with the growth of columnar grains, some equiaxed grains start a free growth in the melt in front of the solidification front by a number of different mechanisms [15]. These free growing grains are pushed toward the end of the mold by the advancement of the solidification front until they form a coherent network of equiaxed dendrites and restricts further longitudinal growth of the columnar grains. This is when CET technically occurs. It seems that faster longitudinal growth of

columnar grains in Chill casting before CET has resulted in a larger columnar zone. In other words, the intrinsic rapid growth of the feathery grains in Chill casting is believed to have balanced its smaller cooling rate (Table 5), leading to increased length of the columnar zone.

3.7.2. Constitutional undercooling

It has been well documented that the growth mode of solidification is controlled by the extent of ΔT_C created in front of a growing interface. The following linear inequality is generally used as the criterion for ΔT_C formation [46].

$$\frac{G}{R} < \frac{mC_S(1-k_0)}{Dk_0} \tag{5}$$

For a specific alloy system, ΔT_C is controlled by the *G/R* ratio and C_S.

During directional solidification of the columnar grains, solute atoms with $k_0 < 1$, e.g. Fe and Cu, are gradually rejected into the remaining liquid to make a progressively enriched solute boundary layer in front of the solid-liquid interface. This will, in turn, increases the C_S and moves the above inequality towards greater ΔT_C values and formation of equiaxed grains and finally CET occurrence.

In order to investigate the relationship between the segregation of solute elements and CET occurrence, Optical Spark Emission (OES) Spectrometry analyses was performed on the central longitudinal

section of the samples at 10 mm spacings. Variation of Cu and Fe concentration along the central horizontal sections of the samples are shown in Fig. 11. Composition of each area was analyzed three times and error of the mean of each data point is shown by an error bar in Fig. 11.

According to Fig. 11a, Cu and Fe concentrations in Chill casting increase continuously to about 4.65 wt% Cu and 0.36 wt% Fe within $x = 0$–50 mm distance from the chiller surface and decreases subsequently. Interestingly, the maximum solute concentration has coincided with the CET occurrence at $x = 48$ mm.

In PCM casting, Cu concentration has steadily increased along the length of the sample from 4.4 to about 4.89 wt%. Fe concentration has followed a similar trend increasing from about 0.34 to 0.38 wt% at the end of the casting. The segregation pattern observed is that normally expected from a directional solidification process [46]. Of course, the minute variation of Fe content along the samples must be treated with caution because it may not be within the detection precision of the spectrometer. In PCM casting, CET has occurred at $x = 35$ mm that corresponds to a Cu concentration of about 4.51 wt%, which is very close to that at the CET of Chill casting, i.e. 4.65 wt%. This may suggest a critical C_S concentration for CET occurrence in Al–Cu alloys and inspires further investigations.

According to Fig. 11c and d, Chill casting has higher Cu and Fe contents than PCM casting up to $x = 50$ mm, and the trend is reversed at larger distances. The difference between the micro-segregation trends of Chill casting and PCM casting may be related to the difference in their growth morphologies.

Higher growth rate of the columnar portion of the Chill casting, i.e. feathery structure, was shown in Table 6. Higher solute content of the columnar zone in this area could be related to solute trapping phenomena, an important phenomenon occurring during rapid solidification or un-equilibrium solidification [47,48]. In such conditions, the alloying elements have less time for diffusion and remain (are trapped) in the solid to form solid solution or intermetallic compounds. It may be hypothesized that segregation in Chill casting is restricted by higher R

induced solute trapping of the feathery structure and, hence, the higher solute content of Chill casting in this area. Consequence of solute trapping would be lower solute rejection in front of the solid-liquid interface, as is evident form Fig. 11. It is interesting that the average Cu and Fe contents of the equiaxed zone in Chill casting is about the original composition of the alloy (Table 1).

Fig. 12 tries to summarize the solidification and solute macrosegregation (yellow curve) paths of both castings. In both castings, first a chill zone and a fine columnar grain zone is formed in contact with the chiller surfaces (Fig. 12a and b). Simultaneous with advancement of the columnar grain zone in each casting, some equiaxed grains may be nucleated in front of the solidification front or some dendrite arms may be separated from the columnar grain zone and transferred to the remaining molten metal. Brighter color in front of the solidification front signifies the higher solute pile-up in that region. At $x = 10$ mm, feathery grains are initiated in the Chill casting due to formation of Fe-rich intermetallic compounds. With time, columnar feathery grains in Chill casting and columnar dendritic grains in PCM casting are progressed toward the end of the castings. At the same time, equiaxed grains in both castings are grown larger and solute pile-up in front of the solidification fronts are intensified (Fig. 12c and d).

Start of melting of the PCM at $x = 30$ mm in PCM casting as well as the increased solute concentration in the remaining melt, result in higher formation and growth rate of the equiaxed grains and, consequently, CET occurrence at $x = 35$ mm in PCM casting (Fig. 12f), while the growth of columnar feathery grains continues in Chill casting (Fig. 12e). CET for Chill casting occurs at $x = 48$ mm (Fig. 12g). Some columnar growth from the end side of the molds is also visible at $x = 48$ mm (Fig. 12g and h). Gradual increase in the melt solute concentration has resulted in gradual increase in the solute content of the solidified part through the k_0 relationship.

3.7.3. Growth restriction factor (GRF)

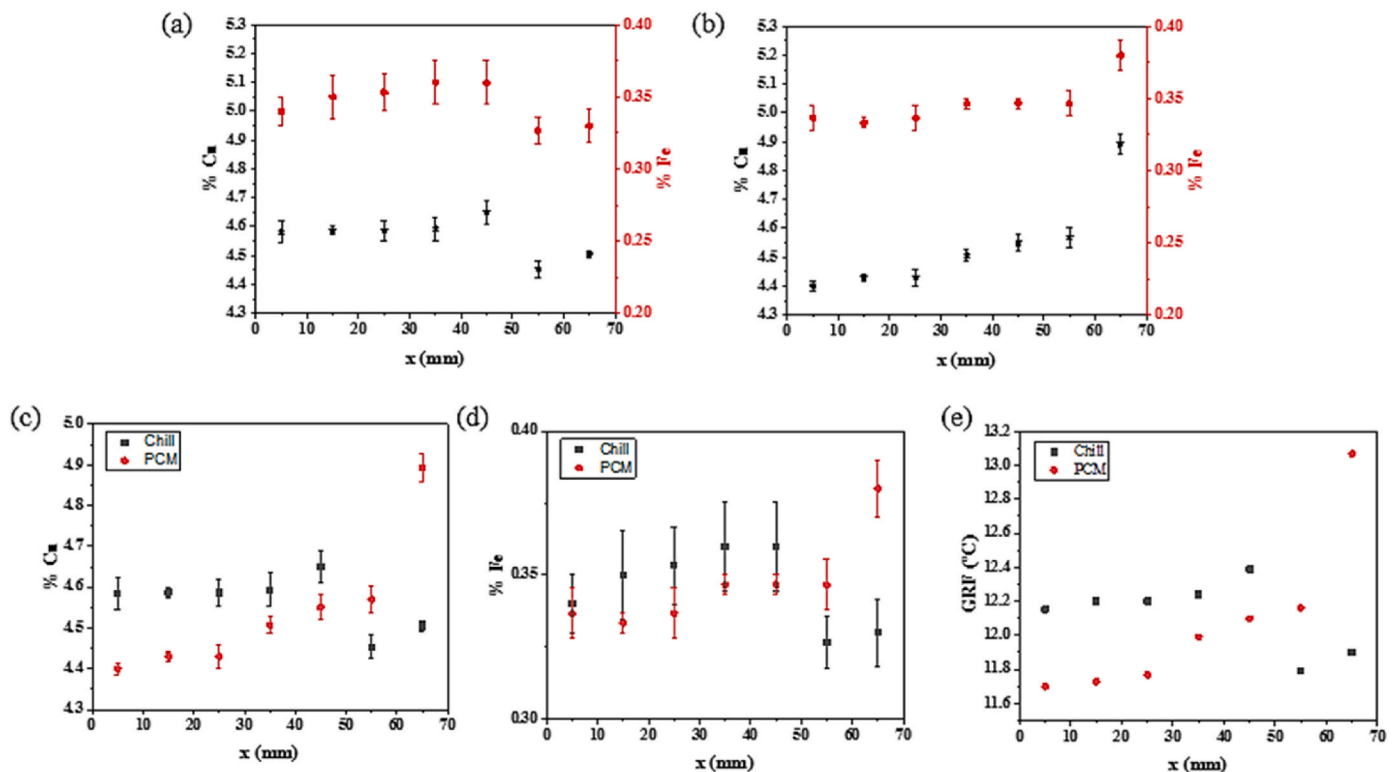Previous research has shown that equiaxed grain formation in front

Fig. 11. Variation of Fe and Cu concentration along central longitudinal section of the samples: (a) Chill casting and (b) PCM casting, as well as comparison of c) Cu concentration, d) Fe concentration and e) GRF values in both castings.
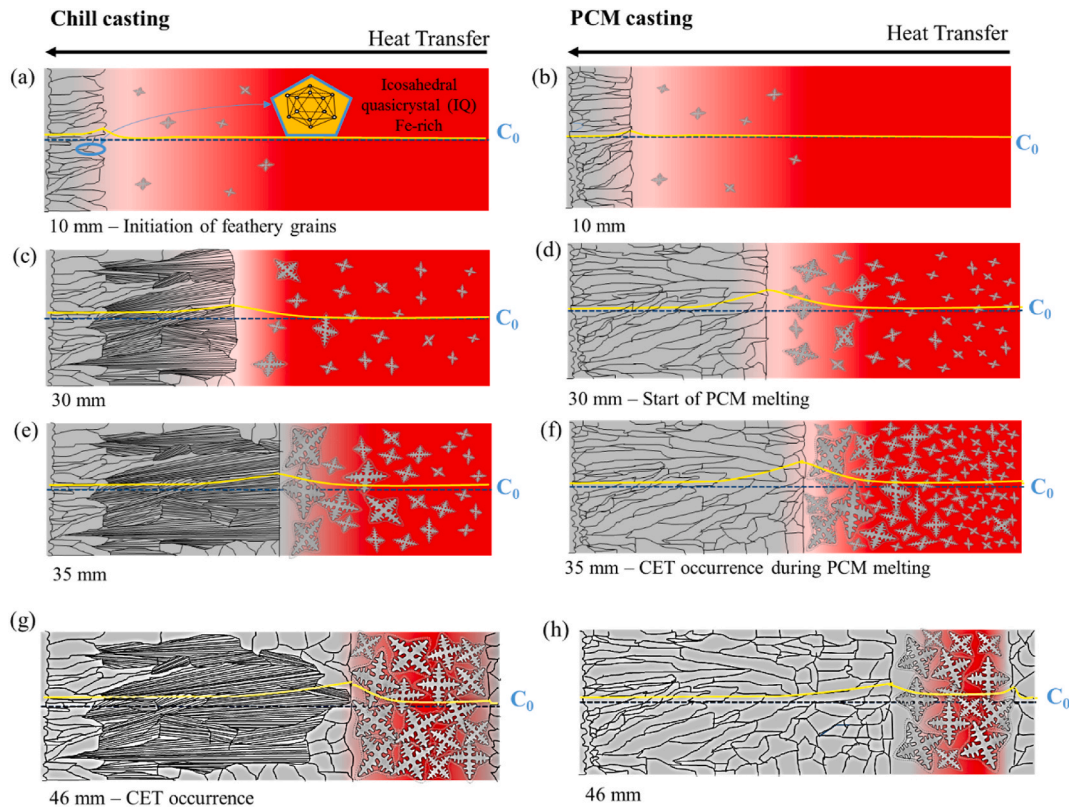
Fig. 12. Schematic representation of solidification and solute macro-segregation in the castings at: a) and b) x = 10 mm, c) and d) x = 30 mm, e) and f) x = 35 mm, and g) and h) x = 48 mm.

of the columnar zone of an alloy is influenced by its GRF because of its influence on formation of the solute concentration layer in front of the solid/liquid interface [20]. In order to investigate the effects of solute segregation on CET occurrence, local GRFs were determined according to the procedure described in section 2.2 and the results are presented in Fig. 11e. Obviously, GRF variation follows the segregation pattern of the solute elements along the casting. Calculation of GRF values for binary Al-4.5 wt%Cu and Al-0.35 wt%Fe compositions indicated GRF values of 10.4 and 1.5, respectively, and suggests that copper is much more effective on CET occurrence than Fe.

3.8. Dendrite arm spacing

Typical micrographs of the columnar zone in Chill and PCM castings are shown in Fig. 13. The characteristic feathery and normal dendritic grains, as discussed before, and their corresponding primary and

secondary arms in Chill and PCM castings are shown in Fig. 13a and b, respectively.

Variation of the PDAS and SDAS along the length of both castings are displayed in Fig. 14. The results indicate a smaller PDAS and SDAS in PCM casting than Chill casting and a steady increase in both PDAS and SDAS from the chillers to the CET zones. The average PDAS values were measured to be about 175 ± 3.2 and 80 ± 4.3 μm in Chill and PCM castings, respectively. As shown in Fig. 14a, PDAS has increased from 67 μm (chiller side) to 690 μm (CET zone) in Chill casting. In PCM casting, it has increase from 62 μm (chiller side) to 400 μm (CET zone). The average SDAS values were 72 ± 5.4 and 43 ± 5 μm in Chill and PCM castings, respectively. As shown in Fig. 14b, SDAS has increased from 58 μm (chiller side) to 86 μm (runner side) in Chill casting and from 27 μm (chiller side) to 57 μm (runner side) in PCM casting. The effects can be explained by to the higher cooling rates experienced in the PCM casting and at the vicinity of the chillers surfaces, as explained earlier.
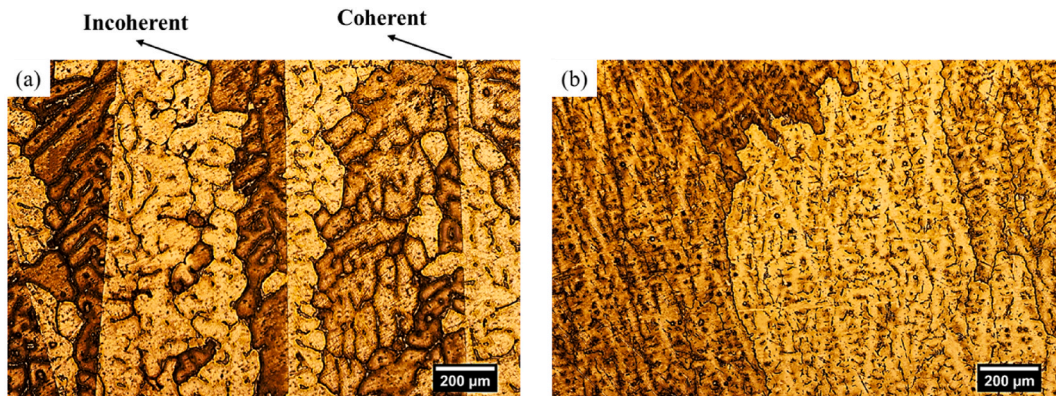

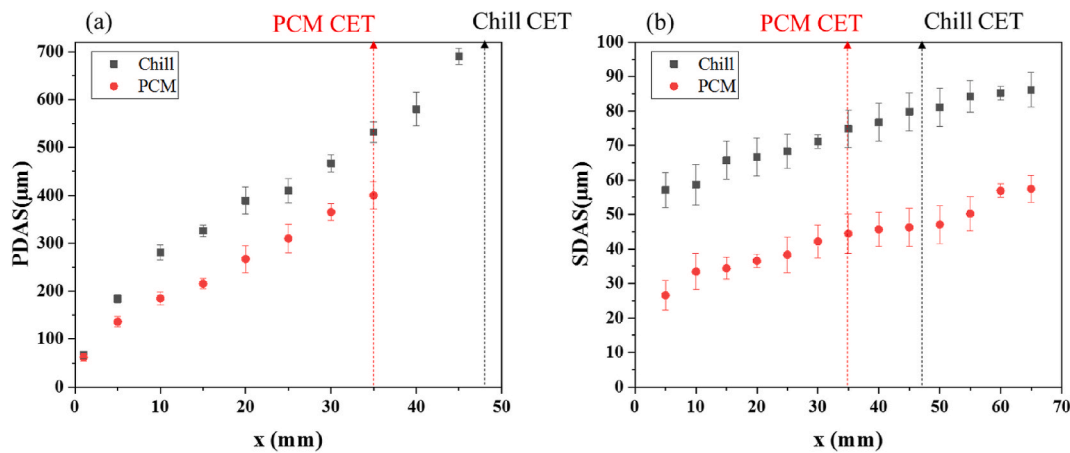**Fig. 13.** Microstructure of columnar zone in a) Chill and b) PCM castings at x = 15 mm.

Fig. 14. Variation of a) PDAS and b) SDAS with distance from the chiller in Chill and PCM castings.

3.9. Shrinkage defects

Typical micrographs exhibiting the extent and distribution of the shrinkage defects formed at different distances from the chillers surfaces in Chill and PCM castings are shown in Figs. 15 and 16, respectively. Shrinkage porosity is formed due to failure of the feeding system to completely compensate the liquid and solidification shrinkages of the casting during solidification. Very often, shrinkage porosity is not formed due to lack of liquid metal in the feeders, but rather due to the limited feeding distance of the feeders. It has been evidently shown that the feeding distance of a feeder can be extended using a suitably located chiller which promotes directional solidification toward the feeder [18].

Fig. 15 indicates that shrinkage defects has been formed from 30 mm distance from the chiller to the end of Chill casting. The defects are, of course, smaller and more widely spaced close to the chiller. On the other hand, more than half of PCM casting is defect free (Fig. 16) and the defects formed in the runner side of PCM casting are less numerous and much smaller than those in Chill casting. These figures clearly show that the PCM fitted chiller has induced a more effective directional solidification toward the feeder due to its more effective cooling.

Overall, the results showed that by using the new generation of metal

chillers introduced, it was possible to modify and refine the solidification structure, accelerate the CET occurrence, control the micro and macro segregation patterns and the type of intermetallic compounds formed, and reduce the shrinkage defects formed in the cast alloys. In the specific work presented here, use of pure Zn as PCM resulted in increased thermal conductivity of the PCM fitted chiller due to higher conductivity of the solid Zn before melting, and improved chiller heat absorption capacity due to melting of the Zn. It is believed that the former avoided the formation of feathery grains and the later resulted in earlier CET occurrence.

3.10. Mechanical properties

The collective effects of this new generation of metal chillers on the macro- and microstructural features of PCM casting are expected to affect its mechanical properties. The average hardness of Chill and PCM castings were measured to be about 60 ± 1.4 and 78 ± 2.2 HB, respectively, confirming the improved mechanical properties of the latter. The hardness profiles along the length of both samples are shown in Fig. 17, where improved hardness of PCM casting is further evident. In Chill casting, the hardness has decrease from about 77 HB (chiller side)
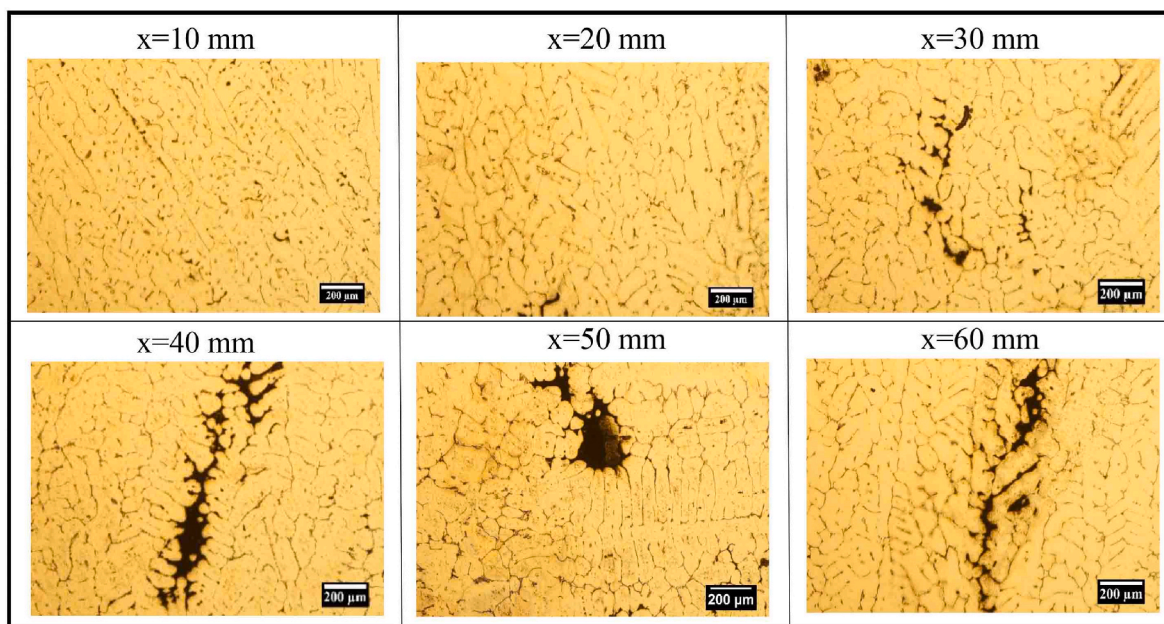

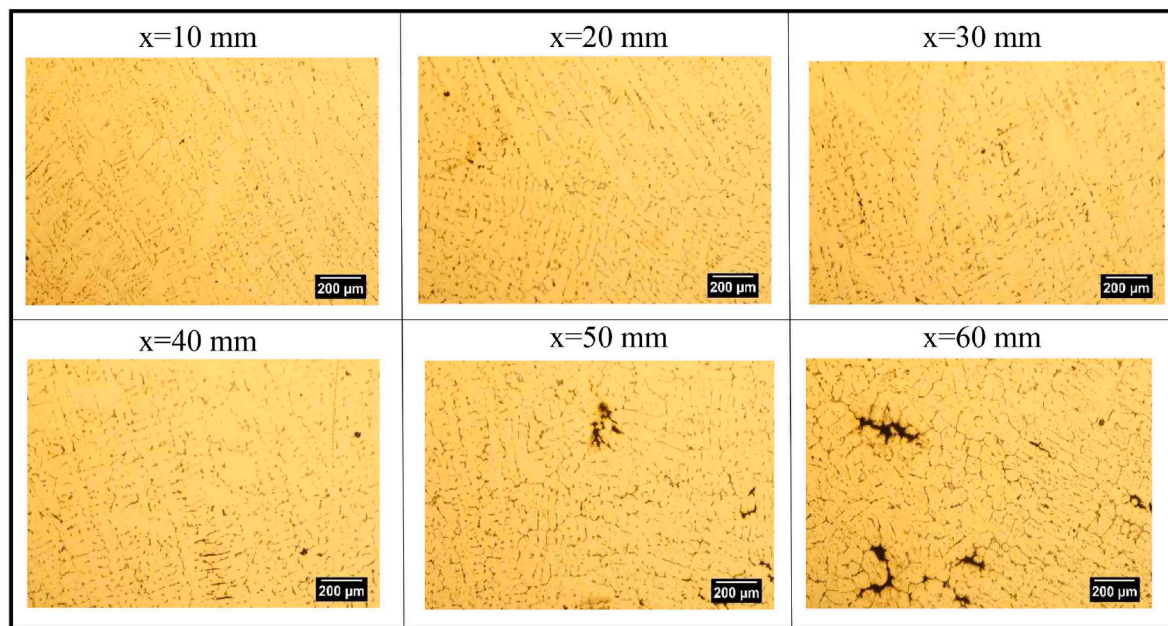**Fig. 15.** Shrinkage porosity distribution in Chill casting.

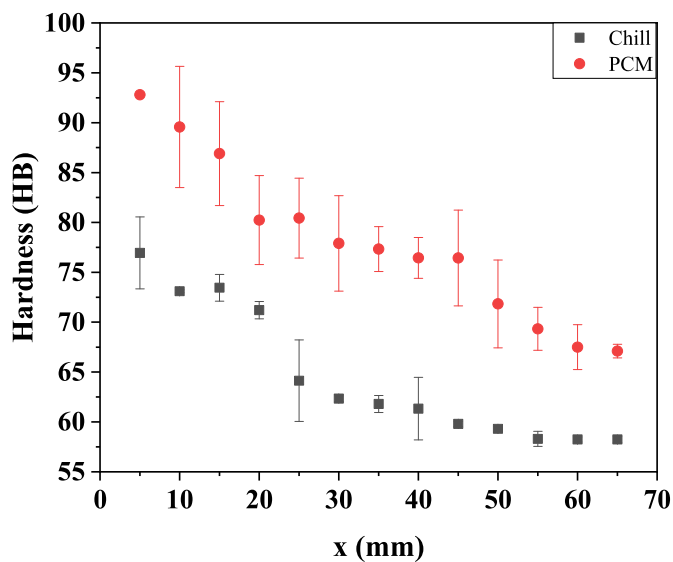**Fig. 16.** Shrinkage porosity distribution in PCM casting.

Fig. 17. Variation of hardness with distance from the chiller in Chill and PCM castings.

to about 58 HB (runner side). In PCM casting, the hardness has decrease from about 93 HB (chiller side) to about 67 HB (runner side). The changes in hardness between the two samples and along the length of each sample follow the changes in the macro- and microstructural features of the castings as discussed in the preceding sections, such as reduced dendrite arm spacing and shrinkage content and changes in the segregation pattern of the solute atoms and morphology of the columnar grains.

3.11. Concluding remarks

Further work is needed to clarify the mechanisms by which modifications in the macro- and microstructure, CET and intermetallic and shrinkage porosity formation in PCM samples take place and to develop tools for selection of PCM and design of the new chiller to tailor the solidification structure of the cast alloys according to the application and services needed.

To sum up, in traditional methods of controlling the solidification structure, such as inoculation, chilling or alloying element addition (GRF modification), the foundryman has no control on the cooling conditions of the castings after pouring. The characteristic gradual decrease in the cooling rate and the thermal gradient in front of the solidification front after pouring results in a typical solidification structure comprised of up to three distinct regions of chill, columnar and central zone of large equiaxed grains.

The findings of this work indicated the potentials of this new generation of chillers in time/temperature sensitive control of the cooling rate of the castings after pouring by careful selection of the type, dimensions and location of PCM fitted chiller(s) strategically planted in the casting molds. This new generation of chillers would be a new practical tool for smart tailoring the cast structure of metallic parts during solidification. Examples of different tailored cast structures of metallic parts which could become feasible using this new generation of metal chillers may include, but not limited to.

- Castings with completely uniform fine equiaxed structures across the castings or with tailored CET occurrence without resort to inoculation or some externally applied processes,
- Castings with coarser grains at the periphery and finer structures in the center,
- Castings with locally refined microstructures,
- Castings with periodic or functionally graded structures across the castings by judicious design and planting of a number of single or multiple type PCM fitted chillers that would become active at given stages of solidification,
- Castings where undesirable features like feathery grains or large intermetallic components have been eliminated,
- Castings with higher integrity structures,
- Castings with less residual stresses, provided the latent heat of solidification of the melted PCM(s) can also be judiciously utilized during the cooling of the castings to the room temperature, and
- Castings with reduced heat treatment requirements due to better structural homogeneity, elimination of undesirable structures such as feathery grains and large or continuous intermetallic components and less residual stresses.

4. Conclusions

A new generation of chillers for control of the solidification structure of cast metals and alloys was examined which utilized the latent heat of melting of pure zinc incorporated in the chiller by experimental and computer simulation investigations. The results demonstrated that.

1. Using the PCM fitted chiller enhanced the thermal conductivity and cooling capacity of the chiller which could be utilized to tailor the macro and microstructural characteristics of cast alloys.
2. Despite the lower cooling rate of Chill casting than that of PCM casting, advancement of the solidification front before melting of the PCM was similar due to high intrinsic growth rate of feathery grains.
3. Formation of feathery grains in directionally solidified Al-4.5 wt%Cu alloy was associated with formation of Al_5Cu_2Fe phase in Fe rich areas of the microstrcuture.
4. Use of the PCM fitted chiller eliminated the formation of the feathery grains and reduced the formation of the undesired Fe-rich phases close to the chiller due to different thermal history of the castings.
5. Use of the PCM fitted chiller resulted in accelerated CET and significantly smaller columnar zone due to latent heat absorption of the pure zinc during solidification of the alloy and affected the solute rejection or entrapment during growth of the solid-liquid interface.
6. Differences in segregation patterns and local GRFs along the castings were related to different cooling and growth conditions experienced by each casting.
7. PDAS, SDAS and shrinkage porosity content of PCM sample were smaller than those of Chill casting which resulted in its improved hardness.
8. Further work is needed to clarify the mechanisms of structural modifications and to develop tools for design of this new generation of chillers to tailor the solidification structure of the cast alloys.

5. Prime Novelty Statement

Several traditional methods, such as chilling, inoculation and vibration, have been used for many decades with very little change to control the solidification structure of cast alloys. In this work, a new generation of metallic chillers for tailoring the solidification structure of cast alloys is introduced and examined. The proposed chiller incorporates one or more phase change materials (PCMs) in a traditionally solid metal chiller. It is shown that using this innovative chiller, morphology, columnar to equiaxed transition (CET) phenomenon and formation of undesirable feathery grains in Al-4.5 wt%Cu alloy could be controlled without any dramatic change in the molding/casting practice and without resort to heat treatment.

Declaration of competing interest

The authors declare that they have no known competing financial interests or personal relationships that could have appeared to influence the work reported in this paper.

References

[1] Berlanga-Labari C, Biezma-Moraleda MV, Rivero PJ. Corrosion of cast aluminum alloys: a review. Metals 2020;10:1–30. https://doi.org/10.3390/met10101384.
[2] Noohi Z, Niroumand B, Timelli G. Numerical simulation of the effects of a phase change material (PCM) on solidification path of gravity sand cast Al-Cu alloy. Metal. Ital. 2023:25.
[3] Mirshahi F, Meratian M, Zahrani MM, Zahrani EM. Effect of cooling rate and chemical modification on the tensile properties of Mg-5wt% Si alloy. Magnes. Technol. 2011:577–82. https://doi.org/10.1002/9781118062029.ch106.
[4] Camicia G, Timelli G. Grain refinement of gravity die cast secondary AlSi7Cu3Mg alloys for automotive cylinder heads. Trans. Nonferrous Met. Soc. China (English Ed. 2016;26:1211–21. https://doi.org/10.1016/S1003-6326(16)64222-X.
[5] Haghayeghi R, Timelli G. An investigation on primary Si refinement by Sr and Sb additions in a hypereutectic Al-Si alloy. Mater Lett 2021;283:128779. https://doi.org/10.1016/j.matlet.2020.128779.
[6] Lu B, Li Y, Wang H, Wang Y, Yu W, Wang Z, Xu G. Effects of cooling rates on the solidification behavior , microstructural evolution and mechanical properties of Al-Zn-Mg-Cu alloys. J Mater Res Technol 2022;22:2532–48. https://doi.org/10.1016/j.jmrt.2022.12.082.
[7] Mirshahi F, Meratian M, Panjepour M. Microstructural and mechanical behavior of Mg/Mg₂Si composite fabricated by a directional solidification system. Mater. Sci. Eng. A 2011;528:8319–23. https://doi.org/10.1016/j.msea.2011.07.057.
[8] Baptista LADS, Paradela KG, Ferreira IL, Garcia A, Ferreira AF. Experimental study of the evolution of tertiary dendritic arms and microsegregation in directionally solidified Al-Si-Cu alloys castings. J Mater Res Technol 2019;8:1515–21. https://doi.org/10.1016/j.jmrt.2018.05.021.
[9] Ashiri R, Niroumand B, Karimzadeh F. Physical, mechanical and dry sliding wear properties of an Al-Si-Mg-Ni-Cu alloy under different processing conditions. J Alloys Compd 2014;582:213–22. https://doi.org/10.1016/j.jallcom.2013.08.016.
[10] Shayan M, Niroumand B, Toroghinejad MR. Effect of applied pressure on mechanical properties of squeeze cast Al-mwcnt composites. Mater. Sci. Technol. Conf. Exhib. 2012;1:128–35. MST 2012 2012.
[11] Fu J, Wang S, Wang K. Influencing factors of the coarsening behaviors for 7075 aluminum alloy in the semi-solid state. J Mater Sci 2018;53:9790–805. https://doi.org/10.1007/s10853-018-2246-z.
[12] Kolahdooz A, Aminian S. Effects of important parameters in the production of Al-A356 alloy by semi-solid forming process. J Mater Res Technol 2019;8:189–98. https://doi.org/10.1016/j.jmrt.2017.11.005.
[13] Nasresfahani MR, Niroumand B, Kermanpur A, Raeissi M. Effects of applied electric current on the tip radius and the universal amplitude coefficient of a single growing dendrite. Surf Rev Lett 2016;23:1–8. https://doi.org/10.1142/S0218625X15500833.
[14] Zhang L, Jiang H, He J, Zhao J. A new model of growth restriction factor for hypoeutectic aluminium alloys. Scr. Mater. 2020;179:99–101. https://doi.org/10.1016/j.scriptamat.2020.01.009.
[15] Davies GJ. Solidification and casting. London: Applied Science Publishers; 1973.
[16] Hunt JD. Steady state columnar and equiaxed growth of dendrites and eutectic. Mater. Sci. Eng. 1984;65:75–83. https://doi.org/10.1016/0025-5416(84)90201-5.
[17] Kurz W, Bezençon C, Gäumann M. Columnar to equiaxed transition in solidification processing. Sci Technol Adv Mater 2001;2:185–91. https://doi.org/10.1016/S1468-6996(01)00047-X.
[18] Campbell J. Complete casting Handbook: metal casting processes. Techniques and Design; 2011. ISBN 978-0-444-63509-9.
[19] Schmid-Fetzer R, Kozlov A. Thermodynamic aspects of grain growth restriction in multicomponent alloy solidification. Acta Mater 2011;59:6133–44. https://doi.org/10.1016/j.actamat.2011.06.026.
[20] Chandrashekar T, Muralidhara MK, Kashyap KT, Rao PR. Effect of growth restricting factor on grain refinement of aluminum alloys. Int J Adv Manuf Technol 2009;40:234–41. https://doi.org/10.1007/s00170-007-1336-x.
[21] Mofijur M, Mahlia TMI, Silitonga AS, Ong HC, Silakhori M, Hasan MH, Putra N, Ashrafur Rahman SM. Phase change materials (PCM) for solar energy usages and storage: an overview. Energies 2019;12:1–20. https://doi.org/10.3390/en12163167.
[22] Liu X, Tie J, Wang Z, Xia Y, Wang CA, Tie S. Improved thermal conductivity and stability of Na2SO410H2O PCMs system by incorporation of Al/C hybrid nanoparticles. J Mater Res Technol 2021;12:982–8. https://doi.org/10.1016/j.jmrt.2021.02.096.
[23] Kandasamy R, Wang XQ, Mujumdar AS. Application of phase change materials in thermal management of electronics. Appl Therm Eng 2007;27:2822–32. https://doi.org/10.1016/j.applthermaleng.2006.12.013.
[24] Noohi Z, Nosouhian S, Niroumand B, Timelli G. Use of low melting point metals and alloys (Tm < 420 °C) as phase change materials: a review. Metals 2022;12:945. https://doi.org/10.3390/met12060945.
[25] Smithells C. J. Metals Reference Book Editor. Elsevier Science; 2013.
[26] Began A, Kraus AD. Heat transfer Handbook. Wiley; 2003.
[27] Noohi Z. Tailoring solidification structure of A-Cu alloy using phase change materials (PCM). Iran: Ph.D. dessertation, Isfahan University of Technology; 2023.
[28] Kurtuldu G, Jarry P, Rappaz M. Influence of Cr on the nucleation of primary Al and Formation of twinned dendrites in Al-Zn-Cr alloys: can icosahedral solid clusters play a role? Acta Mater 2013;61:7098–108. https://doi.org/10.1016/j.actamat.2013.07.056.
[29] Henry S, Jarry P, Jquneau PH, Rappaz M. Electron backscattered diffraction investigation of the texture of feathery crystals in aluminum alloys. Metall. Mater. Trans. A Phys. Metall. Mater. Sci. 1997;28:207–13. https://doi.org/10.1007/s11661-997-0097-3.
[30] Turchin AN, Zuijderwijk M, Pool J, Eskin DG, Katgerman L. Feathery grain growth during solidification under forced flow conditions. Acta Mater 2007;55:3795–801. https://doi.org/10.1016/j.actamat.2007.02.030.
[31] Salgado-Ordorica MA, Valloton J, Rappaz M. Study of twinned dendrite growth stability. Scr. Mater. 2009;61:367–70. https://doi.org/10.1016/j.scriptamat.2009.04.016.
[32] Salgado-Ordorica MA, Twinned Rappaz M. Dendrite growth in binary aluminum alloys. Acta Mater 2008;56:5708–18. https://doi.org/10.1016/j.actamat.2008.07.046.
[33] Meng Y, Cui JZ, Zhao ZH. Effect of Fe on microstructures and mechanical properties of an Al-Mg-Si-Cu-Cr-Zr alloy prepared by low frequency electromagnetic casting. J Mater Res 2017;32:2067–78. https://doi.org/10.1557/jmr.2017.142.

[34] Chen TJ, Li XW, Guo HY, Hao Y. Microstructure and crystal growth direction of Al-Cu alloy. Trans. Nonferrous Met. Soc. China (English Ed. 2015;25:1399–409. https://doi.org/10.1016/S1003-6326(15)63739-6.

[35] Last HR, Sanders TH, Gonsalves JM. Stability of microstructures in chili-cast aluminum alloys containing twinned columnar growth structures. J.M. Gonsalves, Metall. Mater. Trans. A 1990;21:557–65.

[36] Rerko RS, de Groh HC, Beckermann C. Effect of melt convection and solid transport on macrosegregation and grain structure in equiaxed Al-Cu alloys. Mater. Sci. Eng. A 2003;347:186–97. https://doi.org/10.1016/S0921-5093(02)00592-0.

[37] Grushko B, Velikanova TY. Formation of quasicrystals and related structures in systems of aluminum with transition metals. Part 2. Binary systems formed by aluminum with 4d and 5d metals. Poroshkovaya Metall 2004;43:110–22.

[38] Huttunen-Saarivirta E. Microstructure, fabrication and properties of quasicrystalline Al-Cu-Fe alloys: a review. J Alloys Compd 2004;363:154–78. https://doi.org/10.1016/S0925-8388(03)00445-6.

[39] Shabestari SG, Keshavarz M, Hejazi MM. Effect of strontium on the kinetics of formation and segregation of intermetallic compounds in A380 aluminum alloy. J Alloys Compd 2009;477:892–9. https://doi.org/10.1016/j.jallcom.2008.11.037.

[40] Liang G, Ali Y, You G, Zhang MX. Effect of cooling rate on grain refinement of cast aluminium alloys. Materialia 2018;3:113–21. https://doi.org/10.1016/j.mtla.2018.08.008.

[41] Shakiba M, Parson N, Chen XG. Effect of homogenization treatment and silicon content on the microstructure and hot workability of dilute Al-Fe-Si alloys. Mater. Sci. Eng. A 2014;619:180–9. https://doi.org/10.1016/j.msea.2014.09.072.

[42] Zobac O, Kroupa A, Zemanova A, Richter KW. Experimental description of the Al-Cu binary phase diagram. Metall. Mater. Trans. A Phys. Metall. Mater. Sci. 2019; 50:3805–15. https://doi.org/10.1007/s11661-019-05286-x.

[43] Lee N, Cahoon J. Interdiffusion of copper and iron in liquid aluminum. JPED 2011; 32:226–34. https://doi.org/10.1007/s11669-011-9883-0.

[44] Wang L, Sun Y, Bo L, Zuo M, Zhao D. Effects of melt cooling rate on the microstructure and mechanical properties of Al-Cu alloy. Mater Res Express 2019; 6:1–10. https://doi.org/10.1088/2053-1591/ab44eb.

[45] Verma A, Kumar S, Grant PS, O'Reilly KAQ. Influence of cooling rate on the Fe intermetallic formation in an AA6063 Al alloy. J Alloys Compd 2013;555:274–82. https://doi.org/10.1016/j.jallcom.2012.12.077.

[46] Flemings MC. Solidification processing. McGraw Hill; 1974.

[47] Ngomesse F, Reinhart G, Soltani H, Zimmermann G, Browne DJ, Sillekens W, Nguyen-Thi H. In situ investigation of the columnar-to-equiaxed transition during directional solidification of Al–20 Wt.%Cu alloys on earth and in microgravity. Acta Mater 2021;221:117401. https://doi.org/10.1016/j.actamat.2021.117401.

[48] Jabbareh MA, Assadi H. Modelling of microstructure evolution during laser processing of intermetallic containing Ni-Al alloys. Metals 2021;11:1–15. https://doi.org/10.3390/met11071051.